

penetrometer signal using a database containing a range of known weak layer profile segments. If a good match is found, the portion of the signal being analysed is flagged as a possible weak layer. This method is presented as a framework and has not yet been implemented into an operational model.

1.1 Previous work

Wiener spiking deconvolution was developed during WWII by Norbert Wiener to separate radar signals from noise (Leinbach 1995). This technique is commonly used for processing seismic reflection data but has general applications for separating a desired component of a signal of constant sampling interval from unwanted components within that signal. Examples of applications relevant to natural hazards include processing seismic signals from earthquakes, and monitoring volcanism from infrared remote sensing images. Floyer (2003) suggested that this technique might be useful for forecasting avalanches from hourly remote meteorological data.

It is generally accepted that dry slab avalanches initiate in a thin weak layer which lies beneath a thicker, cohesive slab (McClung and Schaerer 2006). Recognizing the presence of weak layers in manual snow profiles as well as the overlying slab properties is therefore fundamental to slab avalanche forecasting. In the absence of direct observations of avalanche occurrences, it is the next most pertinent type of information for assessing the stability of the snowpack (Schweizer *et al.* 2003). McClung (1995) devised a rule-based model to help forecasters assess the stability of a snow profile. Contributions from each of a variety of snow profile attributes including, among others, layer hardness, layer thickness, crystal size and crystal form, were combined using rules devised through a series of interviews with expert forecasters. Schweizer and Jamieson (2003) found that differences between the hardness as well as grain size of the weak layer and adjacent layers were significantly larger for unstable profiles compared with stable profiles. Schweizer and Jamieson (2007) included these variables along with the absolute values for hand hardness and grain size (see Colbeck *et al.* 1990) as well as the Rutschblock score (see McClung and Schaerer 2006) in a model for predicting whether a given snow profile should be considered stable or unstable. They reported prediction levels of 65-77% if the depth to a potential failure plane was known. If the principle weakness was unknown, prediction levels were lower at 53-62%.

Pielmeier and Schweizer (2007) classified potential failure layers in penetrometer signals collected with a SnowMicroPen (SMP) (Schneebeili and Johnson 1998). They found significant differences between certain micromechanical characteristics of the penetrometer signal, the most significant of which was the structural length of the failure layer (Johnson and Schneebeili 1999). Potential failure layers were pre-identified using human interpretation and there was no report on the performance of the classification if the potential failure layers were not pre-identified. Birkeland *et al.* (2004) suggested that a change in

the maximum penetration resistance within a weak layer may indicate an increase in bond strength within that layer.

2. LAYER TRACING

Profiles were collected using a SABRE penetrometer that measures force-resistance using a piezo-electric sensor connected to a 12 mm diameter rounded tip. The profiles were interpolated to a regular depth spacing of 0.05 cm.

For our purposes, we refer to a “layer” as being a small section of a penetrometer profile that contains a definable signal that we are interested in. This section of the signal may represent what we would consider to be an actual snowpack layer, such as a weak layer or a crust, or it may represent an interface between two adjacent snowpack layers.

2.1 Method

The basic steps in the layer tracing method comprise of:

1. Expert identification of the layer (or interface) of interest in the original penetrometer signal.
2. Pre-processing of the penetrometer signals.
3. Wiener spiking deconvolution.
4. Post-processing of the deconvolved output to determine most likely location of the layer of interest in the profile being analysed.

2.1.1 Expert identification of layer of interest

A short, contiguous section of the original penetrometer profile (figure 1a) is defined as the region of interest and this forms the master wavelet, defined as:

$$W = \int_{y_{w_min}}^{y_{w_max}} G_0 dy, \quad [1]$$

where $G_0(y)$ is the original force–depth signal and y_{w_min} and y_{w_max} define the upper and lower boundaries respectively of the layer of interest identified by an expert.

2.1.2 Pre-processing

Pre-processing is done on both the original penetrometer signal, $G_0(y)$ and the penetrometer signal being analysed

$G_a(y)$. We adopt the notation $g_{0,a}^i$ to describe processing steps that are applied to both the original signal and the signal being analysed (subscripts $0,a$). The superscript i denotes, in roman numerals, the order in which these steps are performed. The association with the depth (y) as the independent variable is assumed from here on and dropped from the notation.

A condition of Wiener deconvolution is that there is an identifiable component contained within a signal that is otherwise comprised of random noise. Random noise is characterised by a Gaussian distribution with a mean of zero. In order to approximate this condition, we first remove the broad trend and then apply a high pass filter, which retains the information pertinent for thin-layer or layer-interface identification.

The broad trend was removed from by fitting a least-squares, 4th order polynomial to the signals and retaining the residuals.

$$g_{0,a}^I = G_{0,a} - f_{0,a}, \quad [2]$$

where $f_{0,a} = a_0 + a_1y + \dots + a_4y^4$ and the coefficients a_0 to a_4 are found by minimizing the sum of squares between $G_{0,a}$ and $f_{0,a}$.

A high pass filter was subsequently applied to the trend-removed data. This was applied in the frequency domain using fast Fourier transform (FFT) and inverse FFT methods (e.g. Ifeachor and Jervis 1993, p. 53) to convert to the data into frequency domain and back to the spatial domain respectively.

$$g_{0,a}^{II}(\omega) = (1 - H_H) \times g_{0,a}^I(\omega), \quad [3]$$

where (ω) is used to denote that the filter is applied in the frequency domain and H_H is a Hann window (e.g. Taylor 1994, p. 436) defined as:

$$H_H = \begin{cases} \frac{1}{2} \left(1 + \cos\left(\pi \frac{y}{\tau}\right) \right) & |y| < \tau \\ 0 & otherwise \end{cases} \quad [4]$$

τ is the frequency cut-off parameter used to control which wavelengths are accepted by the filter. We set τ relative to the total depth of the penetrometer signal, d . In practice, for a 200 cm push sampled at an interval of 0.05 cm, setting $\tau = d/2.5$ gave a cut-off wavelength of approximately 8 cm, which worked well. Figure 1 shows how a typical processed signal compares to the unfiltered signal.

2.1.3 Wiener spiking deconvolution

The method of Wiener spiking deconvolution reduces a signal component contained within a signal G to a desired output e by applying an inverse filter a . We find a by defining a wavelet w as the portion of the signal we are trying to find,

in our case, a small portion of the master signal G_0 . We must also specify the desired output e , which we set as a spike marking the start of the layer of interest.

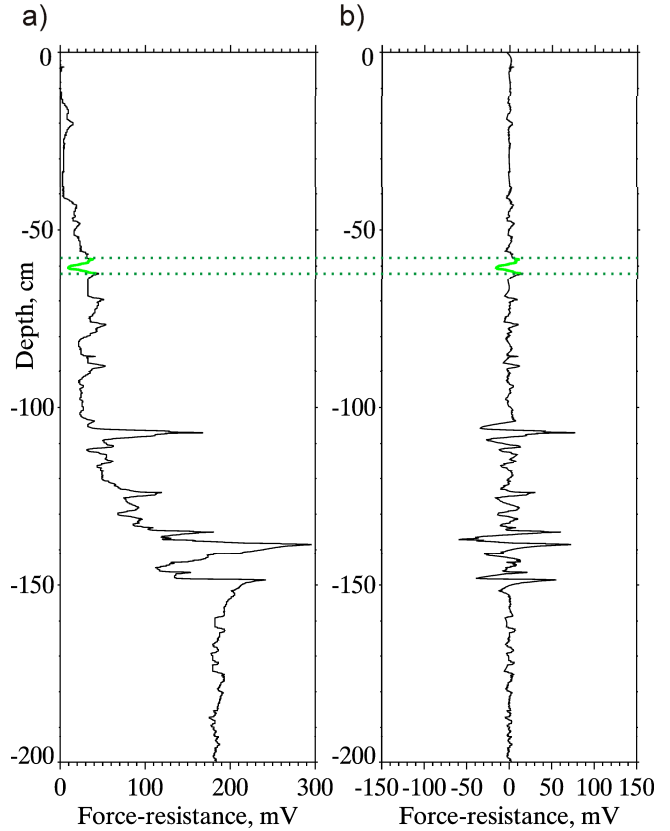


Figure 1. a) Typical unfiltered penetrometer profile. A weak layer is interpreted from this signal at a depth of 60 cm and this is assigned to be the master wavelet. b) Filtered signal from a) with trend removed and a high pass filter applied.

Once we have calculated our inverse filter a , we can use it to search through another signal G_a . If we encounter a section of G_a that is similar to the wavelet w , then the signal at this point will be transformed to a spike that represents the location of this similar layer. If our condition that the rest of the signal comprises of random noise is met (which is not the case, and is discussed in section 2.1.4), then the rest of the signal, which bears no resemblance to w is reduced to 0.

We define the filter a such that:

$$\hat{e} = a * w, \quad [5]$$

where $*$ represents the convolution operator (e.g. Ifeachor and Jervis, 1993, p. 6). \hat{e} is our estimation of the desired output e , which is an n -length vector comprising of a unit spike at e_0 with values at all other points being zero:

$$e = (1, 0, \dots, 0). \quad [6]$$

The wavelet w is defined over the same interval as the master wavelet in equation [1] but is taken from the pre-filtered signal g_0'' :

$$w = \int_{y_{w_min}}^{y_{w_max}} g_0'' dy \quad [7]$$

From Robinson and Treitel (1980), the general form of the matrix equation for an optimum filter a is:

$$\mathbf{R}a = C, \quad [8]$$

where \mathbf{R} is the autocorrelation matrix of the wavelet w and C is the crosscorrelation vector between w and e . In expanded form, this can be written as:

$$\underbrace{\begin{bmatrix} r_0 & r_1 & \dots & r_{n-1} \\ r_1 & r_0 & \dots & r_{n-2} \\ \vdots & \vdots & \ddots & \vdots \\ r_{n-1} & r_{n-2} & \dots & r_0 \end{bmatrix}}_{\mathbf{R}} \underbrace{\begin{bmatrix} a_0 \\ a_1 \\ \vdots \\ a_{n-1} \end{bmatrix}}_a = \underbrace{\begin{bmatrix} c_0 \\ c_1 \\ \vdots \\ c_{n-1} \end{bmatrix}}_C, \quad [9]$$

where subscripts within \mathbf{R} and C represent autocorrelation and crosscorrelation lags respectively.

The inverse filter a is optimal in the sense that it least-squares minimises the error between the actual and desired outputs. This error is given by the scalar \mathcal{E} , summed over the n elements in e :

$$\mathcal{E} = \sum_{i=0}^{n-1} (e_i - \hat{e}_i)^2. \quad [10]$$

For good detection, we must match the energy build-up characteristics of e to the energy build-up characteristics of w . w is said to be a minimum-delay wavelet if all its energy is concentrated towards the front of the wavelet. In this case, we set $e = (1, 0, \dots, 0)$, with the spike at the beginning as in equation [6]. w is said to be a maximum-delay wavelet if all its energy is concentrated towards its end and in this case we modify the desired output to be $e = (0, 0, \dots, 1)$, with the spike at the end of the vector. In the more general

case of a mixed delay wavelet, we iteratively calculate the error from equation [10] for a range of different positions for the spike in e from 0 to $n-1$. The position m that minimises \mathcal{E} is then used to calculate the optimum inverse filter a . If e is varied from its original form in this way, then the final deconvolved output must be offset by m if the spikes are to match up with the start of the layer of interest.

The final step is to use the inverse filter a to deconvolve the signal being analysed. The final deconvolved output is calculated by:

$$\Gamma_a = a * g_a'', \quad [11]$$

2.1.4 Post-processing

If our penetrometer profiles changed in hardness smoothly over the whole range of depths except at the layer of interest, then the pre-processing algorithms in section 2.1.2 would indeed reduce our signal to the layer of interest + random noise approximation. However, the penetrometer profiles that were collected in the Columbia Mountains of British Columbia frequently contain layers of a similar wavelength to that of the layer of interest, but that do not represent the layer we wish to identify. Additionally, it is common in our profiles for the magnitude of the variations to increase with depth. When a layer of the same shape as the master wavelet is encountered but is twice the amplitude, then the resulting spike at this location will be twice as high as the spike generated when the wavelet is deconvolved with itself (termed the wavelet spike from here on). In order to get around this problem, we must further filter the deconvolved data.

In a similar manner to the pre-processing filters, we define post-processing steps $\gamma_{0,a}^i$ that again must be performed in the order described by the roman numeral i . To reduce the effect of high magnitude, short wavelength layers such as crusts that tend to generate spurious detection spikes, we take the difference between the deconvolved output and the wavelet spike and normalize it to unit wavelet spike.

$$\gamma_a^i = \frac{\hat{e} - \sqrt{(\hat{e} - \Gamma_a)^2}}{\hat{e}} \quad [12]$$

Note: if the signal + random noise condition is not closely approximated then we will get better results by replacing \hat{e} in equation [12] with $\Gamma_0 (y = y_{w_min})$.

Since we expect some correlation between the depth of the layer of interest in the original profile and the profile being analysed, we filter the results based on the depth. Our filter comprises of a tapered window, in which we specify a value

of 1 for the depth range where the layer is most likely to be found. The value tapers linearly to zero at both ends of the window over a second range of depths. Both depth ranges that define the window can be customised by the user based on the expected variability between the profiles. The window is applied in the spatial domain and:

$$\gamma_a^{\prime\prime} = H_T \gamma_a^{\prime} \quad [13]$$

where H_T is the tapered window described above.

The final step is to rank the spikes in the filtered, deconvolved output $\gamma_a^{\prime\prime}$. A fully automated implementation of this scheme might simply select the highest ranked spike as the layer of interest, whereas an expert system could present the user with a selection of a small number of likely locations for the layer of interest. Figure 2 shows the original interpreted layer and the traced layer for two different examples; the top 10 ranked spikes are shown in each case.

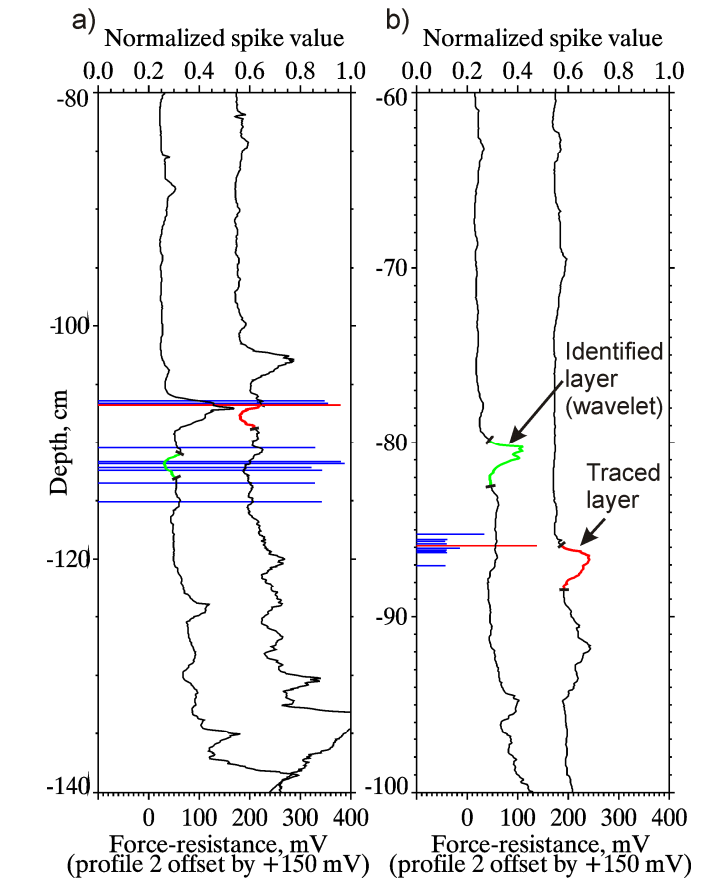
In our implementation of this model, we used the Interactive Data Language (IDL) v6.2. Routines for finding the autocorrelation matrix, and the crosscorrelation matrix and for generating the filter windows were coded from scratch. IDL's built in CONVOL routine was used for performing the convolution operations and the FFT routine was used for performing the fast Fourier transforms. The length of the wavelet has the greatest influence on performance time. On a 1.7 GHz computer running Microsoft Windows XP, processing time for running the layer detection routine on a single profile was approximately 0.25 s for a 3 cm wavelet containing 60 data points and 5 s for an 8 cm wavelet containing 160 data points. Wavelets greater than the wavelength cut-off (8 cm in our case) should not be used.

2.2 Testing the method

The layer tracing algorithm was tested by tracing several layers of interest across two different transects of penetrometer profiles that were collected using our modified SABRE penetrometer. The transects were collected in the winter of 2007 from the Columbia Mountains in British Columbia and each transect comprised of 11 individual profiles. Transect 1 was collected on 21-Feb 2007 on a slope that varied gradually in aspect from NW to NE. Profile spacing for this transect was approximately 2 m. Transect 2 was collected on 15-Mar 2007 on a wind-affected slope with significant variability in snow cover depth. Profile spacing for this transect was approximately 0.5 m.

The layers of interest were grouped into four categories: Crusts (or thin, high resistance layers); weak layers; interfaces (rapid increases in force-resistance); and other layer types that did not fit into the other three categories.

Figure 2. Tracing a layer from the interpreted signal (left signal in each frame) to an un-interpreted signal (right signal



in each frame) for: a) a weak layer and; b) a peak representing a relatively hard layer. The spikes represent the 10 most likely positions for the location of the traced layer. Note that in a) there are several possible positions for the traced layer and the one chosen actually has the third highest spike value. In b) there is only one viable position and the spike value at this point is much greater than the other spikes.

The testing method comprised of identifying a layer of interest in the first profile and then tracing it across subsequent profiles in the transect. Each time a layer of interest was traced to a new profile, the layer that had just been identified became the new reference layer and was assigned as the new master wavelet. In this way, identification of a layer in a new profile was performed using layer information from the closest profile, rather than from the first profile in the transect.

If the layer was judged to have been correctly identified (based on a manual expert comparison between the two signals) by one of the top 10 ranked deconvolution spikes, then this was recorded along with the rank of the spike that best represented the position of the identified layer. If the correct position of the layer was not represented by any of the top 10 ranked deconvolution spikes, then the layer was considered not to have been identified.

2.3 Results

Table 1 shows the number profiles that were correctly identified for each layer that was traced across the transect. Most of the layers were identified quite well, with all but two of the layers showing correct identification for 9-10 out of the possible 10 tracings. (Note: since there were 11 profiles in each transect, there are 10 possible tracings, since the layer was manually identified in the first profile.) We can compare how well each layer was traced by looking at the mean rank of the deconvolution spike for the identified layers. It is clear that crusts, or spikes representing thin high-resistance

layers perform best using this layer-tracing algorithm. The crust layers tested had mean rank values between 1.1 and 2.0. Interfaces between layers of different resistances performed the next best, with those showing a sharp increase in force-resistance performing better than those showing a more gradual increase. The situation for the weak layers was more variable. The low density shallow layer, which was in the relatively quiet, upper part of the signal, performed particularly well, with a mean rank value of 1.2. The weak layer buried 04-Feb 2007 (a surface hoar layer that was recorded with a thickness of 10 mm in a manual profile close to, and on the same day as transect 1) had a

Layer Description	Transect	Number of profiles identified	Number of profiles not identified	Mean rank of spike used for the identification
Crusts				
High density peak ~60 cm	1	10	0	1.1
Lower crust ~ 130cm	1	9	1	1.2
Thin near-surface sun crust	2	10	0	1.2
Double-peaked near-surface crust	2	10	0	1.9
Lower crust ~ 110cm	2	9	1	2.0
Weak layers				
Weak layer (buried 04-Feb 2007)	1	10	0	2.7
Thick (8cm) low density zone	1	1	9	5.0
Low density shallower layer	2	10	0	1.6
Weak Layer (buried 04-Feb 2007)	2	9	1	3.1
Interfaces				
Sharp, high magnitude resistance increase	1	10	0	1.2
Sharp, low magnitude resistance change	1	10	0	2.1
Uneven resistance change	2	10	0	3.4
Other				
Flat portion within layer	1	9	1	3.4
small depression close to crusts	2	0	10	N/A
broad low density layer close to crust	2	8	2	4.5

mean rank value of 2.7 when traced across transect 1. We had less confidence in identifying this layer in transect 2 but we managed to trace a layer which shared characteristics of this layer across transect 2 in all but one profile, with a mean rank value of 3.1. In both cases, this weak layer lay beneath a relatively hard layer that gave a pronounced spike in the signal. It is likely that the proximity of this spike to the weak layer adversely affected the ability to detect this layer. Overall, layers in the "Other" category, which represented fairly nondescript layers, performed the least well compared to the other layer types.

Layers that were not identified well are of interest as they provide insight to the limitations of the method. The thick low density zone was quite a prominent low-resistance layer, although it was characterized by fairly gradual hardness transitions. Since the thickness of this layer was the same as the cut-off wavelength of the high-pass filter (8 cm), it is likely that there was very little residual signal remaining after filtering to allow for unique identification. The other layer that

performed poorly was the broad, low density layer near a crust. Again, its broad nature probably meant that some of its unique characteristics were filtered out and the proximity to the crust was likely responsible for "drowning" the signal at this point with many spurious spikes associated with rapid signal transitions near the crust.

3. WEAK LAYER DETECTION

In the layer-tracing method described above, we assume that a given layer is present in a signal being analysed and we try to find the optimum location for that layer based on values from the deconvolved output. In our layer-detection method, we remove the assumption that a given layer is present and we use the deconvolved output values to indicate the likelihood of finding a particular layer within this signal. We can repeat this task many times using different potential layers that are assigned as the master wavelet.

The steps required for implementing this model are shown schematically in figure 3. We focus on the detection of weak layers since these layers are of particular interest to avalanche forecasters. However, it would be also possible to use this technique to look for crusts or other features within the penetrometer signal. We start by building a database of weak layers from expert interpretation of penetrometer signals combined with knowledge of the prevailing snow stability. Each weak layer wavelet includes the transition from the slab, through the weak layer itself and into the underlying snow. Information about local avalanche conditions, stability test results and other information helpful to avalanche forecasters should be retrievable against the

weak layer wavelets. Next we perform the deconvolution technique outlined in section 2 for all weak layers in the database. In the most general case, we can set the depth filter to be unity for all depth values, making no assumptions about the likely depth of the weak layer. In practice, however, we expect to get better results if we allow detection within a specified range of depths, say ± 15 cm compared to the input weak layer depth. With this assumption, we accept that the shape of a weak layer that causes avalanches at, say, a depth of 40 cm is likely to be different from one that causes avalanches at 100 cm.

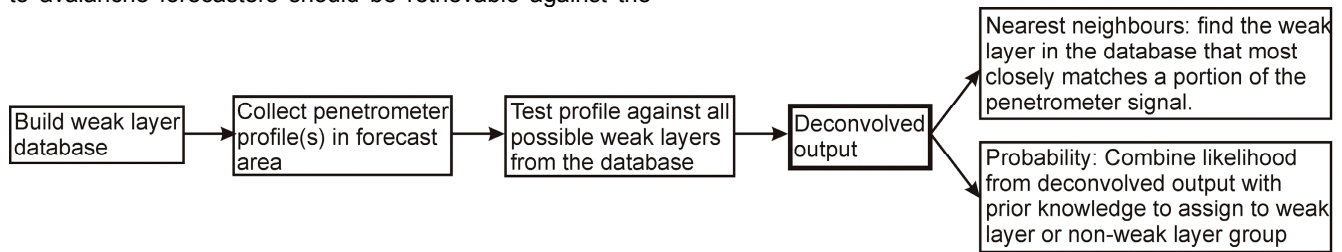


Figure 3. Schematic of the steps involved in the proposed weak layer detection model.

Preliminary testing suggests that detection of similar looking layers from one profile to another profile collected at a different time and place but with similar snowpack characteristics is quite good. We have, however, found that the length of the wavelength has a significant impact on the magnitude of the deconvolved output. It will likely be necessary to fix the number of data points for each wavelet to a uniform value.

In an operational model, the deconvolved output could be used in two possible ways. First, it could be used in a nearest neighbours approach to establish the closest match between the penetrometer signal and the database of potential weak layers. The information about avalanche conditions associated with the highest ranked match could be used by the forecaster to help make a judgment regarding current conditions. Second, the deconvolved output could be assigned as a metric to indicate the likelihood of that point representing a weak layer. The probability density function describing the probability of a given output value representing a weak layer could be generated from a testing set of known weak layers. This framework shares many similarities with an avalanche forecasting scheme presented by McClung and Tweedy (1994), although our initial focus is on forecasting the presence of weak layers rather than direct forecasting of avalanche occurrences. As with McClung and Tweedy's model, the posterior probability for group membership (in our case into weak layer/non-weak layer categories) could be modified using prior expert knowledge. Such knowledge could take the form of an expert opinion of how likely a weak layer was to be found in a given snowpack, a likely depth of burial or likely hardness characteristics of the weak layer and slab.

4. DISCUSSION

Many researchers (Schneebeil *et al.* 1999; Pielmeier and Schneebeil 2003; Kronholm *et al.* 2004) have argued that a vertical resolution in the order of a few micrometres is necessary for reliable weak layer detection from force-resistance penetrometer signals. Although we do not directly dispute this, we argue that significant information can also be gleaned from the broad shape of the weak layer. Analysing the broad shape of the penetrometer signal does not necessitate such high resolution measurements.

Aside from computer performance, which could be significantly enhanced with code optimization, there is no reason why our methods could not be applied to higher resolution penetrometer data, such as that from the SMP. Also, micromechanical information could be combined with an analysis of the shape of the layer. For layer tracing, this could take the form of helping to determine the correct layer in a case where the deconvolved output indicates two or more possible positions of roughly equal likelihood. This could be done by weighting the position which most closely matches the micromechanical characteristics of the layer being traced. For weak layer detection, the posterior probability of a layer being a weak layer could be altered based on a probability density function linking the micromechanical information to the probability of being a weak layer.

5. CONCLUSION

We have presented a method for tracing weak layers across a transect of penetrometer signals and a framework for

extending this method to the problem of generic detection of weak layers in penetrometer signals. For the layer-tracing algorithm, we were successful in tracing layers across the transect in 13 out of the 15 cases in our test. Layers that traced well were crusts, interfaces and weak layers that were not positioned near to a crust. Weak layers that were found near a crust, as well as broader, less distinct features, performed less well in our tests.

The next step will be to build and test the weak layer detection model. This will require populating a database with several known weak layers identified in a range of different penetrometer profiles. The influence of wavelet length on the deconvolved signal output needs to be investigated further. It is also probable that improvements to the pre- and post-filtering will enhance model performance.

Although we designed these techniques with data from a force-resistance penetrometer in mind, there is no reason why they could not also be applied to high-resolution penetrometer signals from other snow properties, such as capacitance and optical reflectivity.

6. ACKNOWLEDGEMENTS

For meticulous field work observations we would like to thank Dave Gauthier, Laura Bakermans, Catherine Brown and Thomas Exner. For support we are grateful to the Natural Sciences and Engineering Research Council of Canada, Helicat Canada, Canadian Avalanche Association, Mike Wiegeler Helicopter Skiing, Canada West Ski Area Association, and Parks Canada. We are grateful to Martin Schneebeli and Karl Birkeland for helpful reviews that improved the quality of this paper.

7. REFERENCES

Abe, O., R. Decker, B. Sensoy, T. Ikarashi, D. Ream and B. Tremper, 1999. Snow profile observations for avalanche forecasts using the new generation rammsonde, *Seppyo no kenkyu (Researches on snow and ice)*, 61(5), 369-375.

Birkeland, K. W., K. Kronholm, M. Schneebeli and C. Pielmeier, 2004. Changes in the shear strength and micro-penetration hardness of a buried surface-hoar layer, *Annals of Glaciology*, 38, 223-228.

Colbeck, S., E. Akitaya, R. Armstrong, H. Gubler, Lafeuille J., K. Lied, D. McClung and E. Morris, 1990. International classification for seasonal snow on the ground, *CRREL Report MP 2794*, International Association of Scientific Hydrology.

Dowd, T. and R. L. Brown, 1986. A new instrument for determining strength profiles in snow cover, *Journal of Glaciology*, 32, 299-301.

Floyer, J. A., 2003. Statistical avalanche forecasting using meteorological data from Bear Pass, British Columbia, Canada, (Master's thesis), University of British Columbia, BC, Canada, 98 pages.

Floyer, J. A., 2006. An update on digital penetrometer technology, *Avalanche.ca - The Journal of the Canadian Avalanche Community*, winter 2006, 14-16.

Ifeachor, E. C. and B. W. Jervis, 1993. Digital Signal Processing, Addison-Wesley.

Johnson, J. B. and M. Schneebeli, 1999. Characterizing the microstructural and micromechanical properties of snow, *Cold Regions Science and Technology*, 30(1-3), 91-100.

Kronholm, K., M. Schneebeli and J. Schweizer, 2004. Spatial variability of micropenetration resistance in snow layers on a small slope, *Annals of Glaciology*, 38, 202-208.

Leinbach, J., 1995. Wiener spiking deconvolution and minimum-phase wavelets; a tutorial, *The Leading Edge*, 14(3), 189-192.

Louge, M. Y., R. L. Foster, N. Jensen and R. Patterson, 1998. A portable capacitance snow sounding instrument, *Cold Regions Science and Technology*, 28, 73-81.

Mackenzie, R. and W. Payten, 2002. A portable, variable-speed, penetrometer for snow pit evaluation, *Proceedings of the International Snow Science Workshop (2002: Penticton, BC)*, 294-300.

McClung, D. M. and P. Schaerer, 2006. The Avalanche Handbook, The Mountaineers, third edition ed., 342 pages.

McClung, D. M., 1995. Use of Knowledge in Avalanche Forecasting, *Defence Science Journal*, 45(2), 117-123.

McClung, D. M. and J. Tweedy, 1994. Numerical avalanche prediction: Kootenay Pass, British Columbia, Canada, *Journal of Glaciology*, 40(135), 350-358.

Pielmeier, C. and M. Schneebeli, 2003. Stratigraphy and changes in hardness of snow measured by hand, ramsonde and snow micro penetrometer: a comparison with planar sections, *Cold Regions Science and Technology*, 37(3), 393-405.

Pielmeier, C. and J. Schweizer, 2007. Snowpack stability information derived from the SnowMicroPen signal, *Cold Regions Science and Technology*, 47(1-2), 102-107.

Robinson, E.A. and S. Treitel, 1980. Geophysical signal analysis, Prentice-Hall, Inc.

Schneebeli, M. and J. B. Johnson, 1998. A constant-speed penetrometer for high-resolution snow stratigraphy, *Annals of Glaciology*, 26, 107-111.

Schneebeli, M., C. Pielmeier and J. B. Johnson, 1999. Measuring snow microstructure and hardness using a high-resolution penetrometer, *Cold Regions Science and Technology*, 30, 101-114.

Schweizer, J. B. Jamieson, 2003. Snowpack properties for snow profile analysis, *Cold Regions Science and Technology*, 37(3), 233-241.

Schweizer, J. and J. B. Jamieson, 2007. A threshold sum approach to stability evaluation of manual snow profiles, *Cold Regions Science and Technology*, 47(1-2), 50-59.

Schweizer, J., J. B. Jamieson and M. Schneebeli, 2003. Snow avalanche formation, *Reviews of Geophysics*, 41(4).

Sihvola, A. and M. Tiuri, 1986. Snow Fork for field determination of density and wetness profiles of a snow pack, *Transactions on Geoscience and Remote Sensing*, GE-24, 717-721.

Taylor, F. J., 1994. Principles of Signals and Systems, McGraw-Hill.